PHYSICAL REVIEW MATERIALS **5**, 034407 (2021)

Neutron study of magnetic correlations in rare-earth-free Mn-Bi magnets

Artem Malyeyev,[1,*] Ivan Titov,[1] Philipp Bender,[1,†] Mathias Bersweiler,[1] Vitaliy Pipich,[2] Sebastian Mühlbauer,[3] Semih Ener,[4] Oliver Gutfleisch,[4] and Andreas Michels[1,‡]

[1]*Department of Physics and Materials Science, University of Luxembourg, 162A Avenue de la Faïencerie, L-1511 Luxembourg, Grand Duchy of Luxembourg*
[2]*Forschungszentrum Jülich GmbH, Jülich Centre for Neutron Science (JCNS) at Heinz Maier-Leibnitz Zentrum (MLZ), Lichtenbergstraße 1, D-85748 Garching, Germany*
[3]*Heinz Maier-Leibnitz Zentrum (MLZ), Technische Universität München, D-85748 Garching, Germany*
[4]*Institute of Materials Science, Technical University of Darmstadt, D-64287 Darmstadt, Germany*

(Received 23 November 2020; revised 20 January 2021; accepted 1 March 2021; published 10 March 2021)

We report the results of an unpolarized small-angle neutron scattering (SANS) study on Mn-Bi-based rare-earth-free permanent magnets. The magnetic SANS cross section is dominated by long-wavelength transversal magnetization fluctuations, and has been analyzed in terms of the Guinier-Porod model and the distance distribution function. This provides the radius of gyration which, in the remanent state, ranges between about $220-240$ nm for the three different alloy compositions investigated. Moreover, computation of the distance distribution function, in conjunction with results for the so-called s parameter obtained from the Guinier-Porod model, indicates that the magnetic scattering of a $Mn_{45}Bi_{55}$ sample has its origin in slightly shape-anisotropic structures.

DOI: 10.1103/PhysRevMaterials.5.034407

I. INTRODUCTION

Permanent magnets are the subject of an intense worldwide research effort, which is due to their technological relevance as integral components in many electronics devices or motors [1,2]. Currently, the worldwide permanent magnet market is dominated by two classes of magnets: (i) High-performance Nd-Fe-B with a maximum energy product of $(BH)_{\max} \cong 400\,\mathrm{kJm^{-3}}$ at 300 K, and (ii) low-performance ferrite magnets with a $(BH)_{\max} \lesssim 40\,\mathrm{kJm^{-3}}$. There is a need for a medium performance and cost effective material working at temperatures as high as 500 K (the typical operating temperature of motors), where the $(BH)_{\max}$ of ternary Nd-Fe-B is unacceptably low; in other words, a low-cost permanent magnet material is required which may replace Nd-Fe-B in such applications where the full potential of the latter is not exploited. Rare-earth-free Mn-based permanent magnets are a prime candidate for filling the gap between Nd-Fe-B and the ferrites [3]. Mn-based magnets in general [4–7], and the low-temperature phase of Mn-Bi binary alloy in particular [8–13], have received a lot of attention lately. This is not in the least because of a positive temperature coefficient of the magnetic anisotropy, rendering high-temperature applications attractive [11].

Most of the published studies on Mn-Bi-based magnets have focused on integral measurement techniques and engineering aspects [14–21]. Yet the macroscopic magnetic properties arise, at least partly, from spatial variations in the magnitude and orientation of the magnetization vector field $\mathbf{M}(\mathbf{r})$ on the mesoscopic length scale (from a few nm up to the micron scale). Therefore, a deeper understanding of the correlations and long-wavelength magnetization fluctuations is of paramount importance both from the basic science point of view, as well as from a materials science perspective which is aiming to optimize the properties of the material.

In this paper we report the results of unpolarized magnetic small-angle neutron scattering (SANS) experiments on cold-compacted isotropic Mn-Bi magnets. The magnetic SANS method is ideally suited to characterize the magnetic structure and interactions on the mesoscopic length scale, since it provides information on both variations of the magnitude and orientation of the magnetization $\mathbf{M}(\mathbf{r})$ in the bulk of the material. This technique has previously been applied to study, e.g., the structures of magnetic nanoparticles [22–32], soft magnetic nanocomposites and complex alloys [33–39], proton domains [40–42], magnetic steels [43–47], or Heusler-type alloys [48–52] (see Ref. [53] for a recent review on magnetic SANS). When conventional SANS is extended by very small-angle neutron scattering, as in the present case, then the accessible real-space length scale may range from a few nanometers up to the micron regime. Here, we aim to estimate the characteristic size of microstructural-defect-induced spin perturbations in the polycrystalline microstructure of Mn-Bi magnets.

The paper is organized as follows: Section II furnishes the details on the sample synthesis and the neutron experiments. Section III displays the expressions for the SANS cross section, the generalized Guinier-Porod model, and the distance

---

[*] artem.malyeyev@uni.lu

[†] Now at: Heinz Maier-Leibnitz Zentrum (MLZ), Technische Universität München, D-85748 Garching, Germany.

[‡] andreas.michels@uni.lu

©2021 American Physical Society

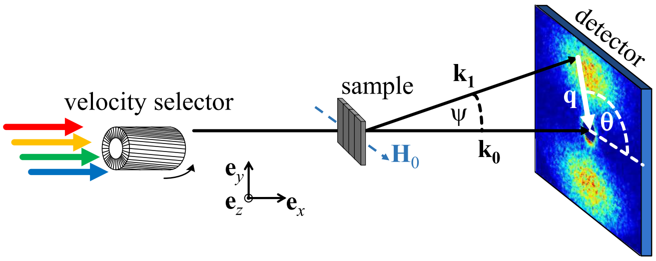

FIG. 1. Sketch of the SANS setup. The external magnetic field to the sample, $\mathbf{H}_0$, is applied perpendicular to the incident neutron beam. The scattering vector $\mathbf{q}$ is defined as the difference between the wave vectors of the incident ($\mathbf{k}_0$) and the scattered ($\mathbf{k}_1$) neutrons, i.e., $\mathbf{q} = \mathbf{k}_0 - \mathbf{k}_1$. Its magnitude for elastic scattering, $q = (4\pi/\lambda)\sin(\psi/2)$, depends on the mean wavelength λ of the neutrons (selected by the velocity selector) and on the scattering angle ψ. The angle θ specifies the orientation of $\mathbf{q}$ on the two-dimensional position-sensitive detector. In the small-angle approximation the component of $\mathbf{q}$ along $\mathbf{k}_0$ is neglected, so that $\mathbf{q} \cong \{0, q_y, q_z\} = q\{0, \sin\theta, \cos\theta\}$ for $\mathbf{H}_0 \perp \mathbf{k}_0$.

distribution function. Section IV then presents and discusses the neutron results. Finally, Sec. V summarizes the main findings of this study. We refer to the Supplemental Material for additional supporting information [54].

II. EXPERIMENTAL DETAILS

All Mn-Bi samples were synthesized by using conventional melting and milling, similar to Refs. [11,55,56]. Initial ingots were prepared by arc melting high-purity elements (99.8 % for Mn and 99.99 % for Bi) and were annealed under an Ar atmosphere for 24 h at 300 °C, followed by quenching in water at room temperature. Subsequently, the resulting ingots were hand crushed under an N_2 atmosphere into powder (with a particle size <60 μm) and ball milled for 2 h in hexane with a ball-to-powder weight ratio of 1:10 at 150 RPM [21]. The ball-milled powder was washed in ethanol, magnetically separated, dried, and cold compacted at a pressure of ∼1.0 GPa into $10 \times 5 \times 1$ mm pellets. Magnetization isotherms were recorded using a vibrating sample magnetometer (Cryogenic, $\mu_0 H_{\max} = 14$ T). For more details on sample preparation and characterization using x-ray diffraction and scanning electron microscopy, see Ref. [55] .

The unpolarized SANS experiments were conducted at room temperature with the very small-angle neutron scattering instrument KWS-3 [57] at the Heinz Maier-Leibnitz Zentrum (MLZ), Garching, Germany. We employed samples grinded down to a thickness of 0.1 mm. The external magnetic field $\mathbf{H}_0$ was applied perpendicular to the incident neutron beam ($\mathbf{H}_0 \perp \mathbf{k}_0$), and a mean wavelength of $\lambda = 12.8$ Å with a bandwidth of $\Delta\lambda/\lambda \cong 10\,\%$ (FWHM) was chosen; see Fig. 1 for a sketch of the neutron setup. The covered momentum transfer ranges between about $0.002\,\mathrm{nm}^{-1} \lesssim q \lesssim 0.2\,\mathrm{nm}^{-1}$. The neutron experiments were performed by first applying a field of 2.2 T and then reducing the field following the magnetization curve (compare Fig. 2). SANS data reduction (correction for background scattering, transmission, and detector efficiency) was carried out using the QTI-SAS software package [58]. Additional neutron measurements on the instrument SANS-1 at MLZ [59] were performed (see Ref. [54] for details).

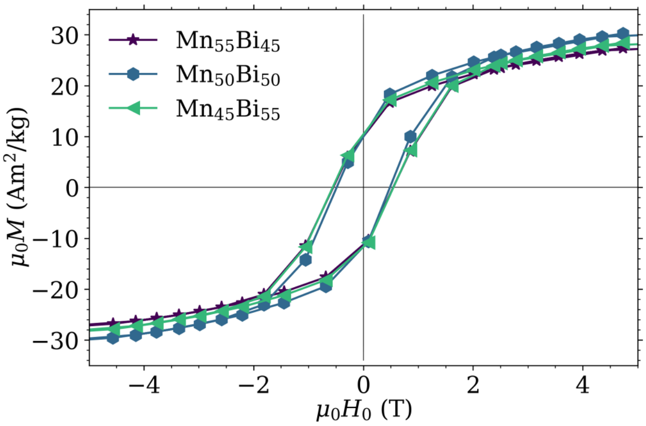

FIG. 2. Room-temperature magnetization curves $M(H_0)$ of various Mn-Bi samples (see inset).

III. SANS CROSS SECTION, GENERALIZED GUINIER-POROD MODEL, AND DISTANCE DISTRIBUTION FUNCTION

In this section the expressions for the unpolarized SANS cross section, the Guinier-Porod model, as well as for the distance distribution function are displayed. For more background details on magnetic SANS, the reader is referred to Refs. [53,60].

A. Unpolarized SANS cross section

For the perpendicular scattering geometry ($\mathbf{H}_0 \perp \mathbf{k}_0$) the elastic unpolarized SANS cross section $d\Sigma/d\Omega$ at momentum-transfer vector $\mathbf{q}$ can be written as [53,60]:

$$\frac{d\Sigma}{d\Omega}(\mathbf{q}) = \frac{8\pi^3}{V} b_H^2 \big(b_H^{-2} |\widetilde{N}|^2 + |\widetilde{M}_x|^2 + |\widetilde{M}_y|^2 \cos^2\theta + |\widetilde{M}_z|^2 \sin^2\theta - (\widetilde{M}_y \widetilde{M}_z^* + \widetilde{M}_y^* \widetilde{M}_z) \sin\theta\cos\theta \big), \tag{1}$$

where V is the scattering volume, $b_H = 2.91 \times 10^8\ \mathrm{A}^{-1}\mathrm{m}^{-1}$ is the magnetic scattering length in the small-angle regime, $\widetilde{N}(\mathbf{q})$ and $\widetilde{\mathbf{M}}(\mathbf{q})$ denote, respectively, the Fourier transforms of the nuclear scattering length density $N(\mathbf{r})$ and the magnetization vector field $\mathbf{M}(\mathbf{r})$, the angle θ is measured between $\mathbf{q}$ and $\mathbf{H}_0$, and the asterisk "∗" marks the complex-conjugated quantity. We would like to emphasize that the magnetization of a bulk ferromagnet is a function of the position $\mathbf{r} = \{x, y, z\}$ inside the material, i.e., $\mathbf{M} = \mathbf{M}(x, y, z)$, and consequently $\widetilde{\mathbf{M}} = \widetilde{\mathbf{M}}(q_x, q_y, q_z)$. However, the above Fourier components represent projections into the plane of the two-dimensional detector, i.e., the q_y-q_z-plane for $\mathbf{H}_0 \perp \mathbf{k}_0$ ($q_x \cong 0$) (compare Fig. 1). This shows that SANS predominantly measures correlations in the plane perpendicular to the incident neutron beam.

In our data analysis we subtract the total nuclear and magnetic SANS cross section at the highest available field from the data at lower fields. This eliminates the nuclear SANS contribution in Eq. (1) and yields the purely magnetic SANS cross section $d\Sigma_M/d\Omega$; to be more precise, the subtraction procedure results in a magnetic SANS cross section which depends on the differences of the magnetization Fourier components at the two fields considered, e.g., $\Delta|\widetilde{M}_x|^2 = |\widetilde{M}_x|^2(H_0) - |\widetilde{M}_x|^2(H_{\max})$ (and similarly for the other Fourier components). The field dependence of the transversal magnetization Fourier components $\widetilde{M}_x$ and $\widetilde{M}_y$ is different from, and usually much larger than, the longitudinal component $\widetilde{M}_z$ (see Fig. 8 in [61]); more specifically, $\widetilde{M}_{x,y}$ are usually larger at lower field than at higher field, whereas $\widetilde{M}_z$ may weakly increase with increasing field. Effectively, for Mn-Bi, this entails that the difference SANS cross section is nonnegative at all $\mathbf{q}$ and H_0 investigated.

B. Generalized Guinier-Porod model

The magnetic SANS cross section $d\Sigma_M/d\Omega$ was analyzed in terms of the generalized Guinier-Porod model, developed by Hammouda [62] in order to describe the 2π-azimuthally-averaged scattering from both spherical and nonspherical objects. The model is purely empirical and essentially decomposes the $I(q) = \frac{d\Sigma_M}{d\Omega}(q)$ curve into a Guinier region for $q \leqslant q_1$ and a Porod region for $q \geqslant q_1$. Both parts of the scattering curve are then joined by demanding the continuity of the Guinier and Porod laws (and of their derivatives) at q_1; more specifically [62]:

$$I(q) = \frac{G}{q^s} \exp\left(-\frac{q^2 R_G^2}{3-s}\right) \quad \text{for} \quad q \leqslant q_1, \tag{2}$$

$$I(q) = \frac{D}{q^n} \quad \text{for} \quad q \geqslant q_1, \tag{3}$$

where the scaling factors G and D, the Guinier radius R_G, the dimensionality factor s, and the Porod power-law exponent n are taken as independent parameters. From the continuity of the Guinier and Porod functions and their derivatives it follows that:

$$q_1 = \frac{1}{R_G}\left[\frac{(n-s)(3-s)}{2}\right]^{1/2}, \tag{4}$$

$$D = G q_1^{n-s} \exp\left(-\frac{q_1^2 R_G^2}{3-s}\right), \tag{5}$$

where $n > s$ and $s < 3$ must be satisfied. Note that q_1 is not a fitting parameter, but an internally computed value [via Eq. (4)]. For a dilute set of homogeneous spherical particles with sharp interfaces, one expects $s = 0$, $n = 4$, and $R_G^2 = \frac{3}{5}R^2$, where R is the particle radius.

C. Distance distribution function

In addition to the above analysis using the generalized Guinier-Porod model, we have model-independently calculated the distance distribution function [63]:

$$p(r) = r^2 \int_0^\infty \frac{d\Sigma_M}{d\Omega}(q) j_0(qr) q^2 dq, \tag{6}$$

where $j_0(qr) = \sin(qr)/(qr)$ denotes the zeroth-order spherical Bessel function. This provides information on the characteristics (e.g., size and shape) of the scattering objects [64,65], and on the presence of interparticle correlations [66,67].

IV. RESULTS AND DISCUSSION

The room-temperature magnetization curves of the Mn-Bi samples are shown in Fig. 2. The coercivity H_c of the samples is found to be between 0.47–0.56 T for all compositions, while the saturation magnetization M_s varies from about 33 Am^2 kg^{-1} ($Mn_{55}Bi_{45}$) to 36 Am^2 kg^{-1} ($Mn_{50}Bi_{50}$) to 34 Am^2 kg^{-1} ($Mn_{45}Bi_{55}$). These values fall short of the theoretical saturation magnetization of the low-temperature Mn-Bi phase (80 Am^2 kg^{-1}) and indicate a magnetic content of ~40 – 45 %. A field larger than 1.8 T is sufficient to close the hysteresis loop and reach the reversible part of the $M(H_0)$ curve. This is important because in the neutron-data analysis the measurement at 2.2 T is used for subtraction to eliminate the nuclear scattering.

Figure 3 illustrates part of our neutron data analysis procedure, which is based on the subtraction of the total $d\Sigma/d\Omega$ at the highest field [Fig. 3(a)] from data at lower fields [Fig. 3(b)]. This eliminates the strong and presumably isotropic nuclear SANS contribution [compare Eq. (1)] and provides access to the purely magnetic SANS cross section $d\Sigma_M/d\Omega$ [Fig. 3(c)] [53,60]. As can be seen in Fig. 4, the $d\Sigma_M/d\Omega$ obtained in this way are anisotropic, elongated along the direction parallel to the applied magnetic field $\mathbf{H}_0$; compare the sector-averaged data in [54]. By comparison to the expression for $d\Sigma/d\Omega$ in the $\mathbf{H}_0 \perp \mathbf{k}_0$ geometry [Eq. (1)], this angular anisotropy can be related to the transversal Fourier component $|\widetilde{M}_y|^2 \cos^2\theta$ in $d\Sigma_M/d\Omega$. The feature is observable for all Mn-Bi samples in the remanent state (Fig. 4), and it suggests the presence of long-range spin-misalignment correlations on a real-space length scale of at least a few tens to a few hundreds of nanometers.

In order to quantify the range of the magnetic correlations, we have azimuthally averaged the two-dimensional magnetic SANS cross sections and fitted the resulting data to the generalized Guinier-Porod (GP) model [Eqs. (2)–(5)]. The results of the weighted nonlinear least-squares fitting procedure for the remanent-state data are displayed in Fig. 5 (solid lines) and demonstrate that the GP model can very well describe the q dependence of $d\Sigma_M/d\Omega$ [54]. The obtained Guinier radii R_G are shown in Fig. 6, while Table I lists (for the remanent state) the results for the remaining fit parameters, the dimensionality parameter s, and the asymptotic power-law exponent n.

The origin of magnetic SANS is due to spatial mesoscale variations in the magnitude and orientation of the magnetization. Such magnetization fluctuations may be caused by microstructural defects (e.g., dislocations, interfaces, pores) via the magnetoelastic coupling of the magnetization to the strain field of the defect [68]. The range and the amplitude of defect-induced spin disorder can be suppressed by an applied field. In the following we associate the value of R_G with the size of such perturbed, nonuniformly magnetized regions around defects.

The Guinier radii in Fig. 6 do not exhibit a systematic variation with the composition of the Mn-Bi samples. At remanence, their values range between $R_G \sim 220 - 240$ nm.

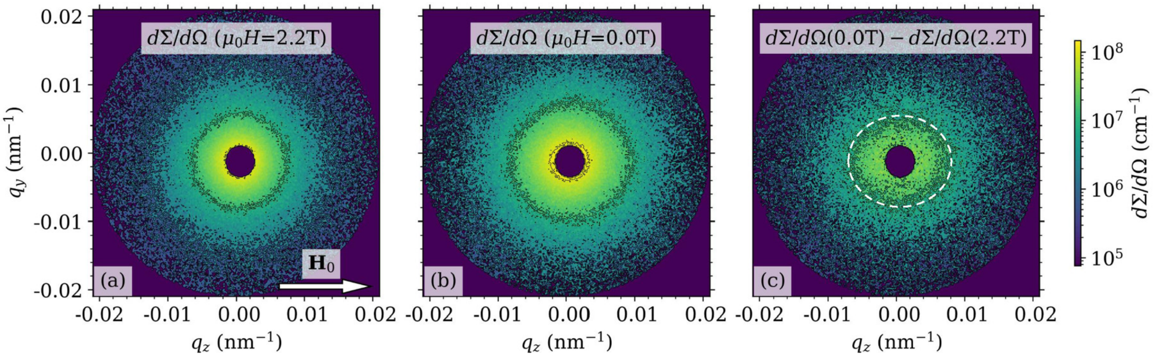

FIG. 3. Illustration of the neutron data analysis procedure. Shown is the total two-dimensional SANS cross section of a $Mn_{55}Bi_{45}$ rare-earth-free permanent magnet ($\mathbf{H}_0 \perp \mathbf{k}_0$; logarithmic color scale). (a) Total (nuclear and magnetic) SANS cross section $d\Sigma/d\Omega$ at $\mu_0 H_0 = 2.2$ T ($\mathbf{H}_0$ is horizontal in the plane, see inset). (b) $d\Sigma/d\Omega$ at remanence (0 T). (c) Magnetic (difference) SANS cross section $d\Sigma_M/d\Omega$ at remanence. The dashed white line emphasizes the slight elongation of $d\Sigma_M/d\Omega$ along $\mathbf{H}_0$ [54].

While the R_G for the $Mn_{55}Bi_{45}$ sample are field independent within error bars, the $Mn_{45}Bi_{55}$ specimen exhibits a decrease of R_G with increasing field, from about 220 nm at remanence to ~100 nm at 1.5 T. Such a behavior is in qualitative agreement with the suppression of spin-misalignment fluctuations around defects with increasing applied field [69]. On the other hand, the $Mn_{50}Bi_{50}$ specimen seems to exhibit an increase of R_G with increasing field, from about 240 nm at remanence to ~285 nm at 1.0 T. However, in view of the large uncertainties in the R_G values of this sample, an unambiguous determination of the field behavior of the $R_G(H_0)$ data set is difficult.

The Porod exponents of $n \sim 3.4 - 3.6$ are systematically reduced below the sharp-interface value of $n = 4$. In the context of particle scattering this observation could be interpreted as a smoothing of the surfaces of the scattering objects [62]. However, for magnetic SANS, where continuous rather than sharp scattering-length density variations are at the origin of the scattering, asymptotic power-law exponents smaller than 4 have only been reported for amorphous magnets [35]. Similarly, exponentially correlated magnetization fluctuations would give rise to $n = 4$, corresponding to a Lorentzian-squared cross section. Therefore, the unusually low n values observed in Mn-Bi remain to be explored by future experimental and theoretical neutron studies.

Within the generalized Guinier-Porod model the s parameter models nonspherical objects [62]. For three-dimensional globular particles (or domains), s is expected to take on a value of $s = 0$. The $Mn_{55}Bi_{45}$ and $Mn_{50}Bi_{50}$ samples are close to this value, whereas $Mn_{45}Bi_{55}$ exhibits $s = 1.07$, which would indicate scattering due to elongated rod-like objects. The latter observation is surprising in view of the fact that extended electron microscopy investigations on similar samples, albeit on a different length scale, did not reveal the presence of shape-anisotropic particles [55].

In order to further understand the differences between the samples (regarding the s parameter), we have model-independently calculated the distance distribution function $p(r)$ [Eq. (6)]. The results for $p(r)$ in Fig. 7 are qualitatively consistent with the numerical fit analysis using the generalized Guinier-Porod model. The $Mn_{55}Bi_{45}$ and $Mn_{50}Bi_{50}$ samples both exhibit a $p(r)$, which is typical for globular scatterers [70]. Yet, a small shoulder at the larger distances points towards the presence of slightly anisotropic structures. By contrast, the $p(r)$ of the $Mn_{45}Bi_{55}$ sample clearly shows a broad maximum at $r \cong 470$ nm followed by a long tail at the larger r, suggesting that the scattering originates from shape-anisotropic elongated objects (compare Fig. 5 in the review by Svergun and Koch [64]). The broad maximum of $p(r)$ at the smaller distances of the $Mn_{45}Bi_{55}$ specimen corresponds to the shorter dimension of the structure. This finding is in line with the behavior of the s parameter obtained from the Guinier-Porod model.

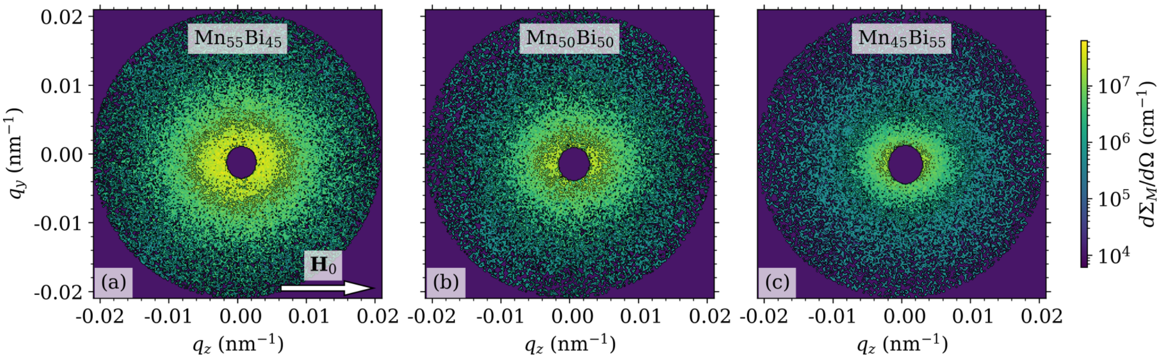

FIG. 4. Two-dimensional magnetic (difference) SANS cross section $d\Sigma_M/d\Omega$ of Mn–Bi rare-earth-free permanent magnets at the remanent state ($\mathbf{H}_0 \perp \mathbf{k}_0$; logarithmic color scale).

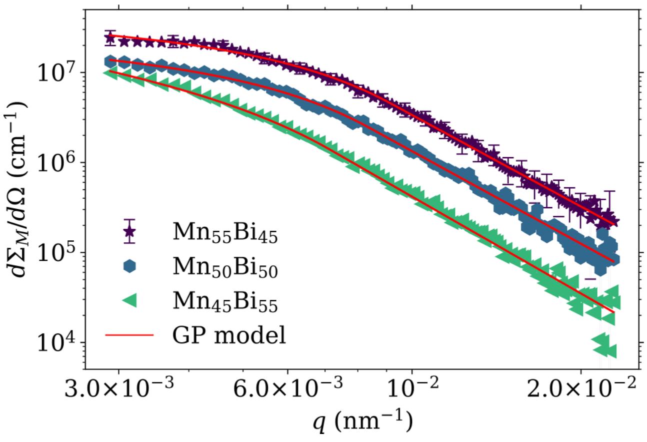

FIG. 5. 2π-azimuthally-averaged $d\Sigma_M/d\Omega$ of Mn–Bi rare-earth-free permanent magnets in the remanent state ($\mathbf{H}_0 \perp \mathbf{k}_0$; log-log scale). Solid lines: Fit to the generalized Guinier-Porod model [Eqs. (2)–(5)]. Error bars are selectively shown only for the $Mn_{55}Bi_{45}$ sample.

TABLE I. Results of the fit analysis on Mn-Bi rare-earth-free permanent magnets using the generalized Guinier-Porod model [62] (remanent state).

	$Mn_{55}Bi_{45}$	$Mn_{50}Bi_{50}$	$Mn_{45}Bi_{55}$
R_G (nm)	224 ± 8	242 ± 12	218 ± 13
s	0.30 ± 0.07	0.35 ± 0.10	1.07 ± 0.09
n	3.38 ± 0.04	3.42 ± 0.04	3.58 ± 0.03

The Guinier radius R_G, which is one of the central outcomes of our neutron analysis (Fig. 6), represents the characteristic size over which microstructural-defect-induced perturbations in the spin structure are transmitted by the exchange interaction into the surrounding crystal lattice; in other words, R_G is considered to be a measure for the size of inhomogeneously magnetized regions around lattice imperfections. This length scale is of relevance for the understanding of the coercivity mechanism in Mn-Bi magnets—domain nucleation versus pinning—which is currently discussed in the literature [56,71,72]. For instance, the nucleation of a reverse domain in a grain usually starts at a defect site, where the magnetic anisotropy may be reduced relative to the bulk phase. Therefore, the presented neutron methodology (analysis of difference data using the generalized Guinier-Porod model and calculation of the distance ditribution function) provides a means to systematically correlate the spin-misalignment length, which is a property of the defect, to the macroscopic parameters (e.g., coercivity, maximum energy product) of a permanent magnet. Moreover, previous studies (e.g., [56]) demonstrated enhanced coercivity over a wide temperature range with shifting alloy composition towards Bi, which was explained by differences in the grain-size distribution. Our SANS analysis indicates that an increase of the Bi content results in increasingly elongated magnetic structures (Fig. 7). Thus, a further increase of Bi might be a valid approach to enhance the magnetic hardness of the compound via shape anisotropy. In this respect, magnetic SANS permits the determination of the relevant figures of merit (R_G, s, n), which are otherwise not accessible by integral measurement techniques.

V. CONCLUSION AND OUTLOOK

We have investigated the magnetic microstructure of rare-earth-free Mn-Bi magnets by means of unpolarized very small-angle neutron scattering (SANS). The magnetic scattering cross section, which has been obtained by subtracting the total nuclear and magnetic scattering signal at 2.2. T from data at lower fields, has been described in terms of the generalized Guinier-Porod model. The value of the Guinier radius is interpreted as the size of inhomogeneously magnetized regions around microstructural defects. We find that the spin-misalignment correlations are in the range of $\sim 100 - 300$ nm for the compositions studied. Moreover, in particular using the distance distribution function, our analysis indicates that the magnetic scattering of the $Mn_{45}Bi_{55}$ sample is related to shape-anisotropic structures, while the

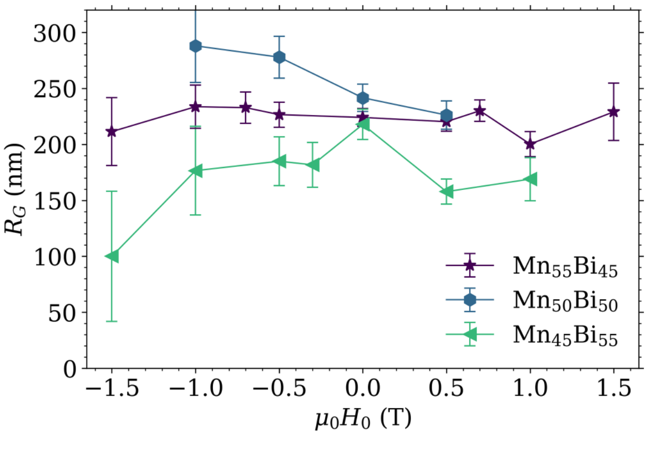

FIG. 6. Magnetic field dependence of the Guinier radii R_G resulting from the generalized Guinier-Porod model. Lines are a guide to the eyes.

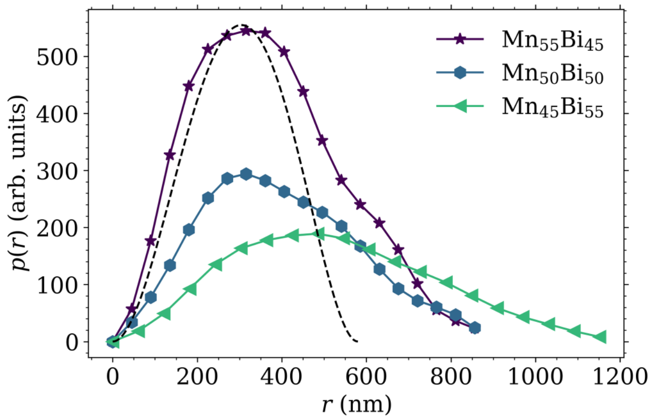

FIG. 7. Distance distribution functions $p(r)$ [Eq. (6)] of the remanent-state Mn-Bi data shown in Fig. 5. Dashed line: Analytical $p(r) \propto r^2(1 - \frac{3r}{4R} + \frac{r^3}{16R^3})$ of a sphere of radius $R = 290$ nm, corresponding to a Guinier radius of $R_G = \sqrt{\frac{3}{5}}R = 225$ nm.

scattering of $Mn_{55}Bi_{45}$ and $Mn_{50}Bi_{50}$ has its origin in more globular-like objects. The neutron-data subtraction procedure (low field minus high field) eliminates the nuclear scattering contribution, which is not further analyzed. In this respect, neutron imaging techniques could be employed for the characterization of the nuclear grain microstructure and morphology inside the bulk of the magnet [73]. In future investigations the use of polarized neutrons will be beneficial (e.g., [26,28,50,74]), since it then becomes possible to directly measure the purely magnetic SANS cross section without the coherent nuclear contribution. Likewise, extending the range of momentum transfers to the so-called ultra SANS regime ($q_{\min} \cong 10^{-4}\ \mathrm{nm}^{-1}$) permits following the correlations up to the 10 micron range. Temperature-dependent neutron measurements will allow one to obtain mesoscale information on the relation between the magnetic microstructure and the positive temperature coefficient of the magnetic anisotropy found for this material.

ACKNOWLEDGMENTS

A.M., P.B., and A. Michels acknowledge financial support from the National Research Fund of Luxembourg (AFR and CORE SANS4NCC grants). We thank the Heinz Maier-Leibnitz Zentrum for the provision of neutron beamtime.

---

[1] O. Gutfleisch, M. A. Willard, E. Brück, C. H. Chen, S. G. Sankar, and J. P. Liu, Adv. Mater. **23**, 821 (2011).

[2] J. R. Riba, C. López-Torres, L. Romeral, and A. Garcia, Renew. Sustain. Energy Rev. **57**, 367 (2016).

[3] J. Coey, Scr. Mater. **67**, 524 (2012).

[4] J. M. D. Coey, J. Phys.: Condens. Matter **26**, 064211 (2014).

[5] S. Ener, K. P. Skokov, D. Y. Karpenkov, M. D. Kuz'min, and O. Gutfleisch, J. Magn. Magn. Mater. **382**, 265 (2015).

[6] H. Jian, K. P. Skokov, and O. Gutfleisch, J. Alloys Compd. **622**, 524 (2015).

[7] Y. Jia, Y. Wu, S. Zhao, S. Zuo, K. P. Skokov, O. Gutfleisch, C. Jiang, and H. Xu, Phys. Rev. Mater. **4**, 094402 (2020).

[8] J. Park, Y.-K. Hong, J. Lee, W. Lee, S.-G. Kim, and C.-J. Choi, Metals **4**, 455 (2014).

[9] V. Ly, X. Wu, L. Smillie, T. Shoji, A. Kato, A. Manabe, and K. Suzuki, J. Alloys Compd. **615**, S285 (2015).

[10] I. Baker, Metals **5**, 1435 (2015).

[11] Y. C. Chen, G. Gregori, A. Leineweber, F. Qu, C. C. Chen, T. Tietze, H. Kronmüller, G. Schütz, and E. Goering, Scr. Mater. **107**, 131 (2015).

[12] S.-M. Kim, H. Moon, H. Jung, S.-M. Kim, H.-S. Lee, H. Choi-Yim, and W. Lee, J. Alloys Compd. **708**, 1245 (2017).

[13] V. V. Nguyen and T. X. Nguyen, Phys. B: Condens. Matter **532**, 103 (2018).

[14] V. V. Nguyen, N. Poudyal, X. B. Liu, J. P. Liu, K. Sun, M. J. Kramer, and J. Cui, Mater. Res. Express **1**, 036108 (2014).

[15] J. Cui, J. P. Choi, E. Polikarpov, M. E. Bowden, W. Xie, G. Li, Z. Nie, N. Zarkevich, M. J. Kramer, and D. Johnson, Acta Mater. **79**, 374 (2014).

[16] N. Poudyal, X. Liu, W. Wang, V. V. Nguyen, Y. Ma, K. Gandha, K. Elkins, J. P. Liu, K. Sun, M. J. Kramer, and J. Cui, AIP Adv. **6**, 056004 (2016).

[17] Y. Mitsui, K. I. Abematsu, R. Y. Umetsu, K. Takahashi, and K. Koyama, J. Magn. Magn. Mater. **400**, 304 (2016).

[18] Z. Xiang, Y. Song, D. Pan, Y. Shen, L. Qian, Z. Luo, Y. Liu, H. Yang, H. Yan, and W. Lu, J. Alloys Compd. **744**, 432 (2018).

[19] Z. Xiang, C. Xu, T. Wang, Y. Song, H. Yang, and W. Lu, Intermetallics **101**, 13 (2018).

[20] I. Janotová, P. Švec Sr., P. Švec, I. Mat'ko, D. Janičkovič, B. Kunca, J. Marcin, and I. Škorvánek, J. Alloys Compd. **749**, 128 (2018).

[21] J. Cao, Y. L. Huang, Y. H. Hou, Z. Q. Shi, X. T. Yan, Z. C. Zhong, and G. P. Wang, J. Magn. Magn. Mater. **473**, 505 (2019).

[22] S. Disch, E. Wetterskog, R. P. Hermann, A. Wiedenmann, U. Vainio, G. Salazar-Alvarez, L. Bergström, and T. Brückel, New J. Phys. **14**, 013025 (2012).

[23] A. Günther, D. Honecker, J.-P. Bick, P. Szary, C. D. Dewhurst, U. Keiderling, A. V. Feoktystov, A. Tschöpe, R. Birringer, and A. Michels, J. Appl. Cryst. **47**, 992 (2014).

[24] P. Bender, A. Günther, D. Honecker, A. Wiedenmann, S. Disch, A. Tschöpe, A. Michels, and R. Birringer, Nanoscale **7**, 17122 (2015).

[25] P. Bender, J. Fock, C. Frandsen, M. F. Hansen, C. Balceris, F. Ludwig, O. Posth, E. Wetterskog, L. K. Bogart, P. Southern, W. Szczerba, L. Zeng, K. Witte, C. Grüttner, F. Westphal, D. Honecker, D. González-Alonso, L. Fernández Barquín, and C. Johansson, J. Phys. Chem. C **122**, 3068 (2018).

[26] P. Bender, E. Wetterskog, D. Honecker, J. Fock, C. Frandsen, C. Moerland, L. K. Bogart, O. Posth, W. Szczerba, H. Gavilán, R. Costo, M. T. Fernández-Díaz, D. González-Alonso, L. Fernández Barquín, and C. Johansson, Phys. Rev. B **98**, 224420 (2018).

[27] S. D. Oberdick, A. Abdelgawad, C. Moya, S. Mesbahi-Vasey, D. Kepaptsoglou, V. K. Lazarov, R. F. L. Evans, D. Meilak, E. Skoropata, J. van Lierop, I. Hunt-Isaak, H. Pan, Y. Ijiri, K. L. Krycka, J. A. Borchers, and S. A. Majetich, Sci. Rep. **8**, 3425 (2018).

[28] Y. Ijiri, K. L. Krycka, I. Hunt-Isaak, H. Pan, J. Hsieh, J. A. Borchers, J. J. Rhyne, S. D. Oberdick, A. Abdelgawad, and S. A. Majetich, Phys. Rev. B **99**, 094421 (2019).

[29] P. Bender, D. Honecker, and L. F. Barquín, Appl. Phys. Lett. **115**, 132406 (2019).

[30] M. Bersweiler, P. Bender, L. G. Vivas, M. Albino, M. Petrecca, S. Mühlbauer, S. Erokhin, D. Berkov, C. Sangregorio, and A. Michels, Phys. Rev. B **100**, 144434 (2019).

[31] D. Zákutná, D. Nižňanský, L. C. Barnsley, E. Babcock, Z. Salhi, A. Feoktystov, D. Honecker, and S. Disch, Phys. Rev. X **10**, 031019 (2020).

[32] L. G. Vivas, R. Yanes, D. Berkov, S. Erokhin, M. Bersweiler, D. Honecker, P. Bender, and A. Michels, Phys. Rev. Lett. **125**, 117201 (2020).

[33] N. Ito, A. Michels, J. Kohlbrecher, J. S. Garitaonandia, K. Suzuki, and J. D. Cashion, J. Magn. Magn. Mater. **316**, 458 (2007).

[34] S. Saranu, A. Grob, J. Weissmüller, and U. Herr, Phys. Status Solidi A **205**, 1774 (2008).

[35] D. Mettus, M. Deckarm, A. Leibner, R. Birringer, M. Stolpe, R. Busch, D. Honecker, J. Kohlbrecher, P. Hautle, N. Niketic, J. R. Fernández, L. F. Barquín, and A. Michels, Phys. Rev. Mater. **1**, 074403 (2017).

[36] I. Mirebeau, N. Martin, M. Deutsch, L. J. Bannenberg, C. Pappas, G. Chaboussant, R. Cubitt, C. Decorse, and A. O. Leonov, Phys. Rev. B **98**, 014420 (2018).

[37] A. Schroeder, S. Bhattarai, A. Gebretsadik, H. Adawi, J.-G. Lussier, and K. L. Krycka, AIP Adv. **10**, 015036 (2020).

[38] M. Bersweiler, P. Bender, I. Peral, L. Eichenberger, M. Hehn, V. Polewczyk, S. Mühlbauer, and A. Michels, J. Phys. D: Appl. Phys. **53**, 335302 (2020).

[39] Y. Oba, N. Adachi, Y. Todaka, E. P. Gilbert, and H. Mamiya, Phys. Rev. Research **2**, 033473 (2020).

[40] B. van den Brandt, H. Glättli, I. Grillo, P. Hautle, H. Jouve, J. Kohlbrecher, J. A. Konter, E. Leymarie, S. Mango, R. P. May, A. Michels, H. B. Stuhrmann, and O. Zimmer, Eur. Phys. J. B **49**, 157 (2006).

[41] V. K. Aswal, B. van den Brandt, P. Hautle, J. Kohlbrecher, J. A. Konter, A. Michels, F. M. Piegsa, J. Stahn, S. Van Petegem, and O. Zimmer, Nucl. Instrum. Methods Phys. Res. A **586**, 86 (2008).

[42] Y. Noda, S. Koizumi, T. Masui, R. Mashita, H. Kishimoto, D. Yamaguchi, T. Kumada, S.-i. Takata, K. Ohishi, and J. Suzuki, J. Appl. Cryst. **49**, 2036 (2016).

[43] M. Bischof, P. Staron, A. Michels, P. Granitzer, K. Rumpf, H. Leitner, C. Scheu, and H. Clemens, Acta Mater. **55**, 2637 (2007).

[44] F. Bergner, C. Pareige, V. Kuksenko, L. Malerba, P. Pareige, A. Ulbricht, and A. Wagner, J. Nucl. Mater. **442**, 463 (2013).

[45] R. Pareja, P. Parente, A. Muñoz, A. Radulescu, and V. de Castro, Philos. Mag. **95**, 2450 (2015).

[46] Y. Oba, S. Morooka, K. Ohishi, N. Sato, R. Inoue, N. Adachi, J. Suzuki, T. Tsuchiyama, E. P. Gilbert, and M. Sugiyama, J. Appl. Cryst. **49**, 1659 (2016).

[47] S. Shu, B. D. Wirth, P. B. Wells, D. D. Morgan, and G. R. Odette, Acta Mater. **146**, 237 (2018).

[48] K. P. Bhatti, S. El-Khatib, V. Srivastava, R. D. James, and C. Leighton, Phys. Rev. B **85**, 134450 (2012).

[49] V. V. Runov, Yu. P. Chernenkov, M. K. Runova, V. G. Gavrilyuk, N. I. Glavatska, A. G. Goukasov, V. V. Koledov, V. G. Shavrov, and V. V. Khovaĭlo, J. Exp. Theo. Phys. **102**, 102 (2006).

[50] G. Benacchio, I. Titov, A. Malyeyev, I. Peral, M. Bersweiler, P. Bender, D. Mettus, D. Honecker, E. P. Gilbert, M. Coduri, A. Heinemann, S. Mühlbauer, A. Çakır, M. Acet, and A. Michels, Phys. Rev. B **99**, 184422 (2019).

[51] S. El-Khatib, K. P. Bhatti, V. Srivastava, R. D. James, and C. Leighton, Phys. Rev. Mater. **3**, 104413 (2019).

[52] S. K. Sarkar, S. Ahlawat, S. D. Kaushik, P. D. Babu, D. Sen, D. Honecker, and A. Biswas, J. Phys.: Condens. Matter **32**, 115801 (2020).

[53] S. Mühlbauer, D. Honecker, É. A. Périgo, F. Bergner, S. Disch, A. Heinemann, S. Erokhin, D. Berkov, C. Leighton, M. R. Eskildsen, and A. Michels, Rev. Mod. Phys. **91**, 015004 (2019).

[54] See Supplemental Material at http://link.aps.org/supplemental/10.1103/PhysRevMaterials.5.034407 for further neutron data.

[55] Y.-C. Chen, S. Sawatzki, S. Ener, H. Sepehri-Amin, A. Leineweber, G. Gregori, F. Qu, S. Muralidhar, T. Ohkubo, K. Hono, O. Gutfleisch, H. Kronmüller, G. Schütz, and E. Goering, AIP Adv. **6**, 125301 (2016).

[56] S. Muralidhar, J. Gräfe, Y.-C. Chen, M. Etter, G. Gregori, S. Ener, S. Sawatzki, K. Hono, O. Gutfleisch, H. Kronmüller, G. Schütz, and E. J. Goering, Phys. Rev. B **95**, 024413 (2017).

[57] V. Pipich and Z. Fu, Journal of Large-Scale Research Facilities **1**, A31 (2015).

[58] V. Pipich, QtiSAS/QtiKWS Visualisation, Reduction, Analysis and Fit Framework with Focus on Small Angle Scattering, http://qtisas.com (2018).

[59] S. Mühlbauer, A. Heinemann, A. Wilhelm, L. Karge, A. Ostermann, I. Defendi, A. Schreyer, W. Petry, and R. Gilles, Nucl. Instrum. Methods Phys. Res. A **832**, 297 (2016).

[60] A. Michels, J. Phys.: Condens. Matter **26**, 383201 (2014).

[61] A. Michels, S. Erokhin, D. Berkov, and N. Gorn, J. Magn. Magn. Mater. **350**, 55 (2014).

[62] B. Hammouda, J. Appl. Crystallogr. **43**, 716 (2010).

[63] P. Bender, L. K. Bogart, O. Posth, W. Szczerba, S. E. Rogers, A. Castro, L. Nilsson, L. J. Zeng, A. Sugunan, J. Sommertune, A. Fornara, D. González-Alonso, L. Fernández Barquín, and C. Johansson, Sci. Rep. **7**, 45990 (2017).

[64] D. I. Svergun and M. H. J. Koch, Rep. Prog. Phys. **66**, 1735 (2003).

[65] G. Fritz and O. Glatter, J. Phys.: Condens. Matter **18**, S2403 (2006).

[66] P. Lang and O. Glatter, Langmuir **12**, 1193 (1996).

[67] G. Fritz-Popovski, A. Bergmann, and O. Glatter, Phys. Chem. Chem. Phys. **13**, 5872 (2011).

[68] H. Kronmüller and M. Fähnle, *Micromagnetism and the Microstructure of Ferromagnetic Solids* (Cambridge University Press, Cambridge, 2003).

[69] D. Mettus and A. Michels, J. Appl. Cryst. **48**, 1437 (2015).

[70] Note that for these two samples the respective maximum of the $p(r)$ function, which is indicative of the "particle" radius R, roughly agrees with the R_G value computed according to $R_G^2 = \frac{3}{5}R^2$ (assuming a spherical particle shape).

[71] C. Curcio, E. S. Olivetti, L. Martino, M. Küpferling, and V. Basso, Phys. Procedia **75**, 1230 (2015).

[72] J. Zamora, I. Betancourt, and I. A. Figueroa, J. Supercond. Nov. Magn. **31**, 873 (2018).

[73] T. Wroblewski, E. Jansen, W. Schäfer, and R. Skowronek, Nucl. Instrum. Methods Phys. Res. A **423**, 428 (1999).

[74] S. M. Yusuf, J. M. De Teresa, M. D. Mukadam, J. Kohlbrecher, M. R. Ibarra, J. Arbiol, P. Sharma, and S. K. Kulshreshtha, Phys. Rev. B **74**, 224428 (2006).

Supplemental Material to "Neutron study of magnetic correlations in rare-earth-free Mn–Bi magnets"

Artem Malyeyev,[1,*] Ivan Titov,[1] Philipp Bender,[1,†] Mathias Bersweiler,[1] Vitaliy Pipich,[2]
Sebastian Mühlbauer,[3] Semih Ener,[4] Oliver Gutfleisch,[4] and Andreas Michels[1,‡]

[1]*Department of Physics and Materials Science,*
University of Luxembourg, 162A Avenue de la Faïencerie,
L-1511 Luxembourg, Grand Duchy of Luxembourg
[2]*Forschungszentrum Jülich GmbH, Jülich Centre for Neutron*
Science (JCNS) at Heinz Maier-Leibnitz Zentrum (MLZ),
Lichtenbergstraße 1, D-85748 Garching, Germany
[3]*Heinz Maier-Leibnitz Zentrum (MLZ),*
Technische Universität München, D-85748 Garching, Germany
[4]*Institute of Materials Science, Technical University*
of Darmstadt, D-64287 Darmstadt, Germany

Abstract

In this Supplemental Material we provide additional neutron data in support of the above paper. More specifically, the data shown below clearly reveal that on a wide range of momentum transfers q (from about $0.003\,\mathrm{nm}^{-1}$ to $0.2\,\mathrm{nm}^{-1}$) and, hence, real-space length scale, the magnetic SANS cross section is dominated by long-wavelength *transversal* spin misalignment. The scattering is enhanced along the direction of the applied magnetic field $\mathbf{H}_0$ (compare the term $|\widetilde{M}_y|^2 \cos^2\theta$ in Eq. (1) in the main paper), resulting in a ratio of horizontal-to-vertical scattering that is larger than the isotropic value of 1 (compare Figs. 3 and 6).

---

[*] artem.malyeyev@uni.lu

[†] Now at: Heinz Maier-Leibnitz Zentrum (MLZ), Technische Universität München, D-85748 Garching, Germany

[‡] andreas.michels@uni.lu

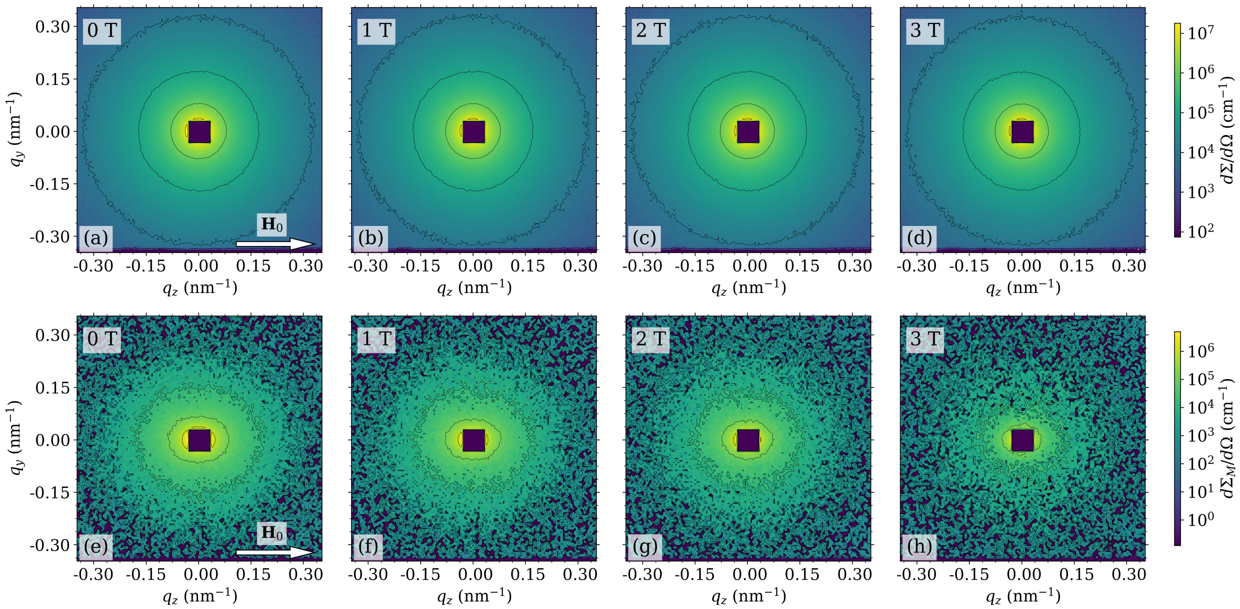

FIG. 1. Field dependence of the two-dimensional SANS cross section of $Mn_{55}Bi_{45}$ rare-earth-free permanent magnet ($\mathbf{H}_0 \perp \mathbf{k}_0$; logarithmic color scale; data measured at SANS-1, MLZ). (a)−(d) Total nuclear and magnetic $d\Sigma/d\Omega$. (e)−(h) Magnetic SANS cross section $d\Sigma_M/d\Omega$, obtained by subtracting the $d\Sigma/d\Omega$ at 4 T from the data at lower fields.

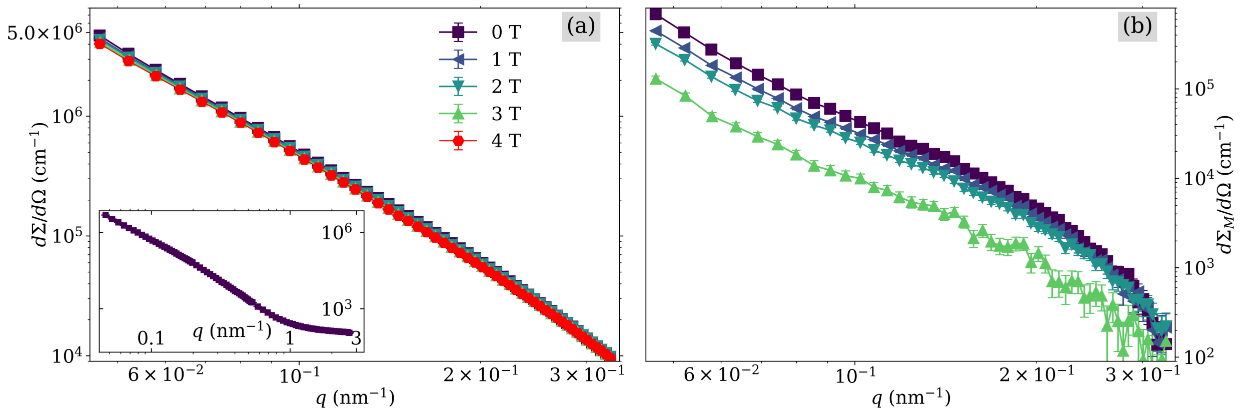

FIG. 2. 2π-azimuthal-average of the data shown in Fig. 1 (log-log scale). (a) $d\Sigma/d\Omega$; (b) $d\Sigma_M/d\Omega$. Lines are guide to the eyes. Inset in (a) shows the full q-dependence of $d\Sigma/d\Omega$.

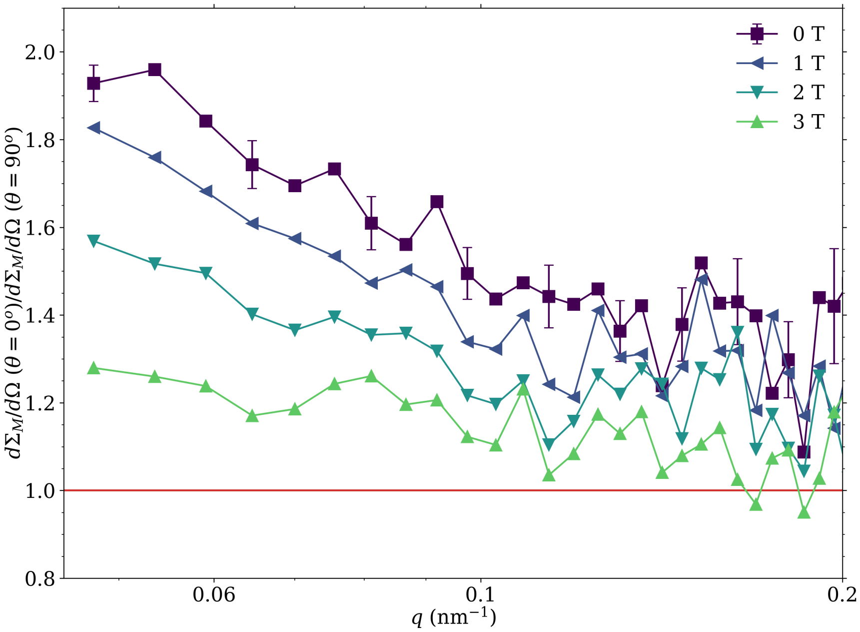

FIG. 3. Ratio of horizontal-to-vertical scattering (log-linear scale; $\mathbf{H}_0 \perp \mathbf{k}_0$). Data [from Fig. 1(e)−(h)] correspond to ±8° sector averages along the horizontal ($\theta = 0°$) and vertical ($\theta = 90°$) directions. Horizontal line corresponds to isotropic scattering. Lines are guide to the eyes.

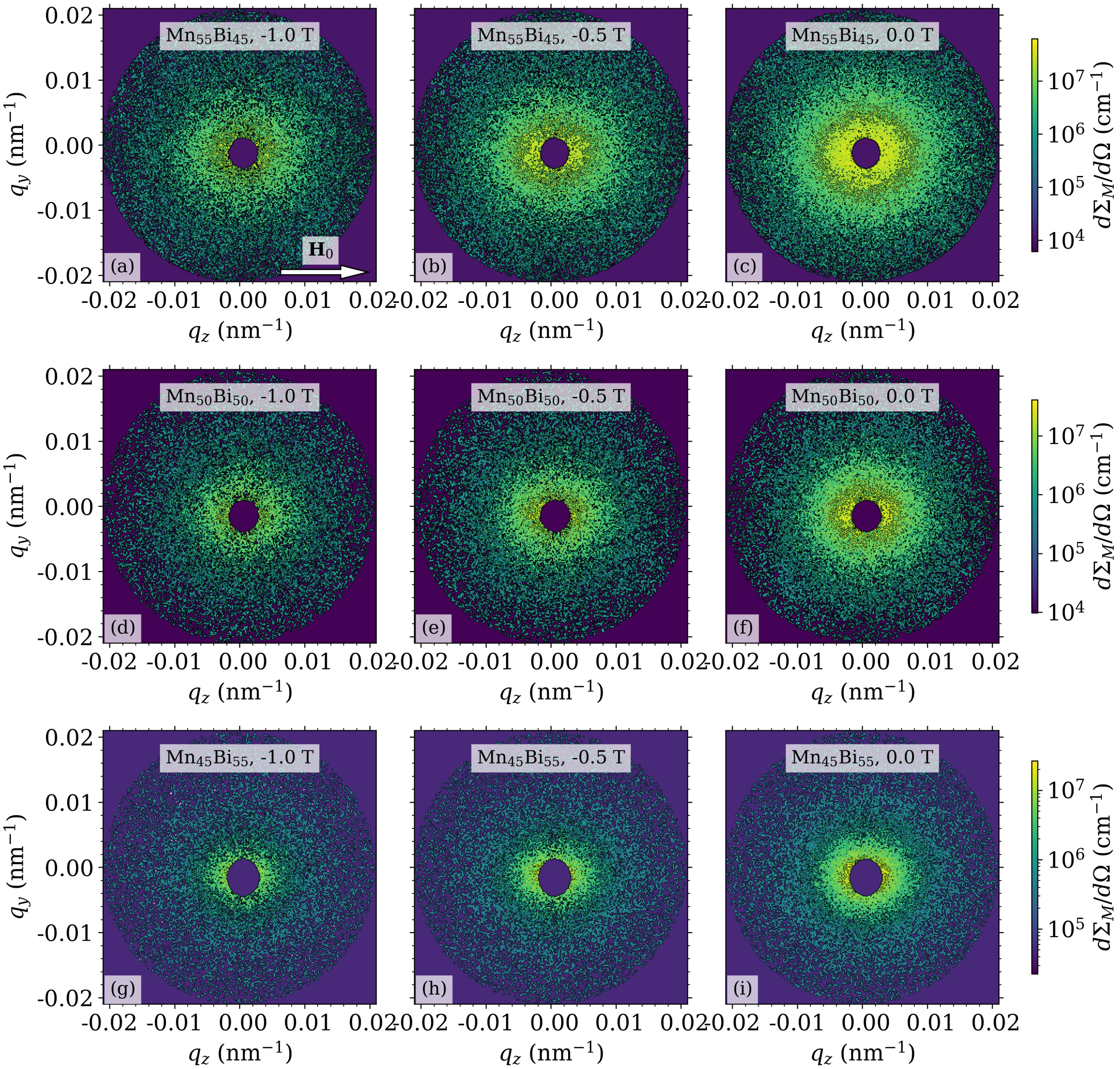

FIG. 4. Field dependence of the two-dimensional magnetic SANS cross section $d\Sigma_M/d\Omega$ of Mn–Bi rare-earth-free permanent magnets ($\mathbf{H}_0 \perp \mathbf{k}_0$; logarithmic color scale; data measured at KWS-3, MLZ). The $d\Sigma_M/d\Omega$ are obtained by subtracting the $d\Sigma/d\Omega$ at 2.2 T from the data at lower fields.

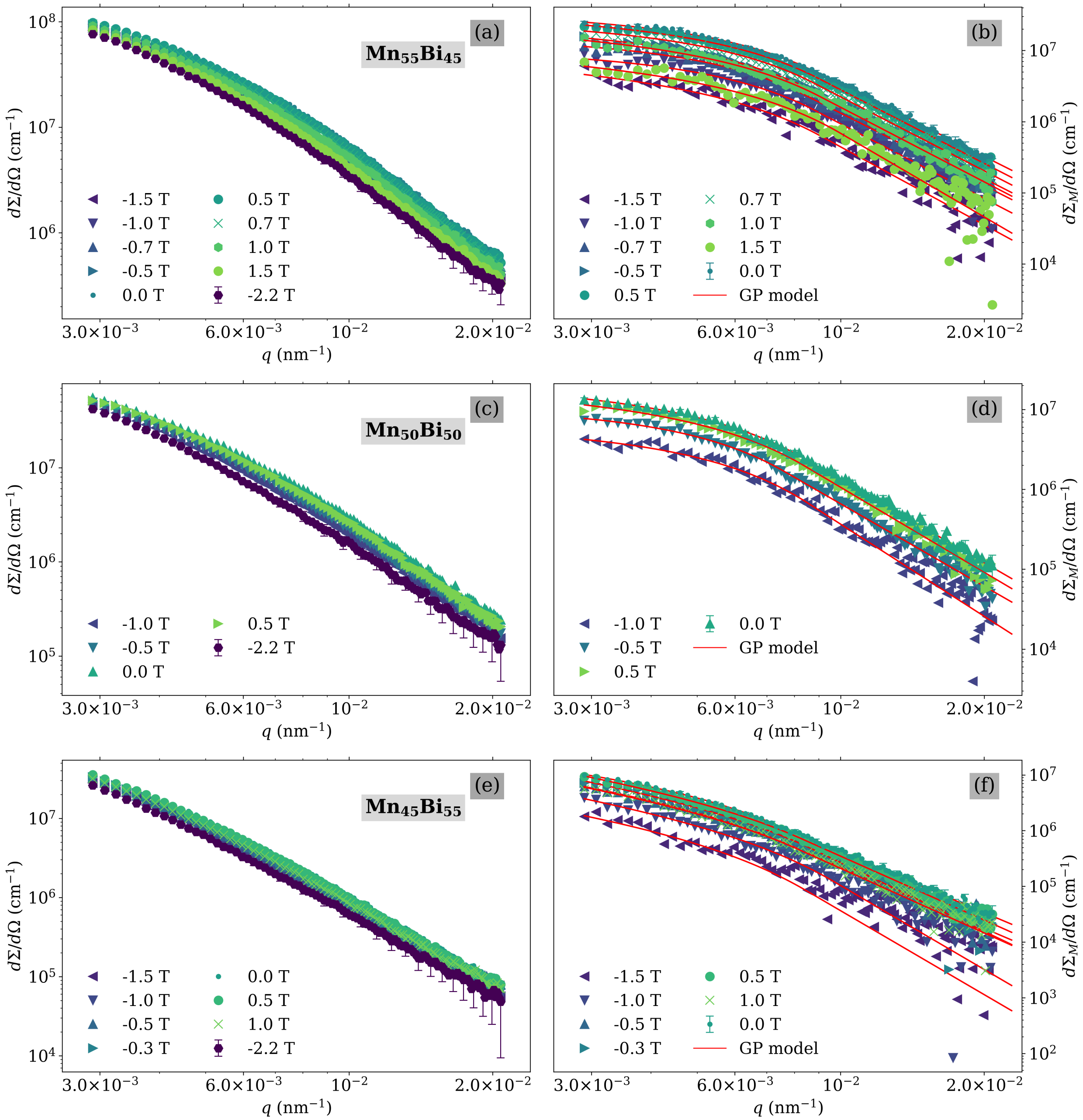

FIG. 5. Field dependence of the 2π-azimuthally-averaged SANS cross sections of Mn–Bi magnets ($\mathbf{H}_0 \perp \mathbf{k}_0$; log-log scale; data measured at KWS-3, MLZ). (a),(c),(e) Total nuclear and magnetic $d\Sigma/d\Omega$. (b),(d),(f) Magnetic SANS cross section $d\Sigma_M/d\Omega$, obtained by subtracting the $d\Sigma/d\Omega$ at 2.2 T. Solid lines in (b),(d),(f): Fit to the generalized Guinier-Porod model.

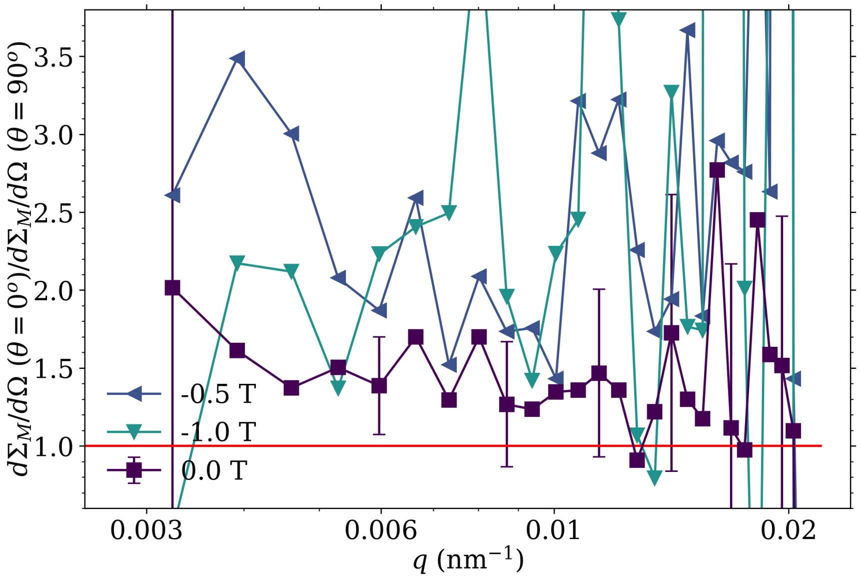

FIG. 6. Ratio of horizontal-to-vertical scattering (log-linear scale; $\mathbf{H}_0 \perp \mathbf{k}_0$). Data correspond to ±8° sector averages along the horizonal ($\theta = 0°$) and vertical ($\theta = 90°$) directions [compare Fig. 4(a)−(c)]. Horizontal line corresponds to isotropic scattering. Lines are guide to the eyes. The here shown data extend the results shown in Fig. 3 to smaller momentum transfers q.